Evaluation of Sonic Boom Shock Wave Generation with CFD Methods

aerospace

MDPI

Article

Evaluation of Sonic Boom Shock Wave Generation with CFD Methods

Samuele Graziani [1,*], Francesco Petrosino [2], Jacob Jäschke [3], Antimo Glorioso [4], Roberta Fusaro [1] and Nicole Viola [1]

[1] Mechanical and Aerospace Engineering Department, Politecnico di Torino, 10129 Torino, Italy; roberta.fusaro@polito.it (R.F.); nicole.viola@polito.it (N.V.)
[2] Italian Aerospace Research Center (CIRA), 81043 Capua, Italy; f.petrosino@cira.it
[3] Institute of Air Transportation Systems, Hamburg University of Technology, 21073 Hamburg, Germany; jacob.jaeschke@tuhh.de
[4] Engineering Department, Università degli Studi della Campania "Luigi Vanvitelli", 81031 Aversa, Italy; antimo.glorioso@unicampania.it
* Correspondence: samuele.graziani@polito.it

Abstract: Over the past two decades, there has been a renewed interest in the development of a new generation of supersonic aircraft for civil purposes that could potentially succeed Concorde. However, the noise annoyance is still considered one of the hampering factors to meet public consensus. This paper aims at revealing the potential of numerical simulations to predict sonic boom signature in Near Field at early design stages. In particular, the paper further demonstrates the applicability of the numerical approach proposed by NASA and other partners during the Sonic Boom Prediction Workshops held between 2014 and 2021, to compute the pressure signature of aircraft in the zone close to it. The results highlight the suitability of the approach (1) to capture the impact of aircraft flight condition variations on the sonic boom signature, (2) to enable the characterization of novel aircraft layout, including Mach 5 waverider configuration, (3) to provide near-field shock wave noise predictions that can be used to evaluate shock propagation, on-ground signature analyses, and annoyance assessment.

Keywords: aeroacoustics; sonic boom; CFD; shock wave

Citation: Graziani, S.; Petrosino, F.; Jäschke, J.; Glorioso, A.; Fusaro, R.; Viola, N. Evaluation of Sonic Boom Shock Wave Generation with CFD Methods. *Aerospace* **2024**, *11*, 484. https://doi.org/10.3390/aerospace11060484

Academic Editor: Bo Zhang

Received: 30 April 2024
Revised: 10 June 2024
Accepted: 17 June 2024
Published: 19 June 2024

1. Introduction

There has been a rising interest in the development of a new generation of supersonic aircraft for civil purposes as the demand for such aircraft would probably allow economically viable operations under specific circumstances [1]. Different conceptual designs for future supersonic aircraft are under investigation ([2–4]), but to this day, none of them have entered operations. The challenge to reintroduce commercial supersonic flight persists mainly due to environmental issues and related effects on the public, e.g., reducing exhaust emissions and lowering the noise impact.

Due to sonic boom annoyance, supersonic flight over land is prohibited in most countries today [5]. On the other hand, the ability to fly over land at supersonic speeds is considered crucial to the economic success of these configurations.

As one of the biggest challenges for supersonic aircraft development remains the mitigation of the noise generated by the shock waves around the aircraft, also known as a sonic boom [6], this paper aims to further understand the generation of sonic boom shock waves at supersonic speeds for different aircraft configurations, including a Concorde-like layout and a waverider.

Over the past decades, numerous technologies and techniques have been developed to improve the prediction of sonic boom events [7] and to minimize sonic boom loudness such that it falls within possible future imposed limits [8]. Those limits are difficult to achieve with large aircraft due to their requirements in terms of volume and lift [9].

With the growing interest in a new generation of sustainable supersonic aircraft, there is increasing activity in the study of new innovative supersonic aircraft concepts that can actually meet future sustainability requirements. The definition of an acceptable sonic boom level produced by supersonic aircraft for the population is one of the most important tasks for regulatory agencies to ensure that these configurations can fly at supersonic speeds in the future [5].

Recently, NASA has put huge effort into the realization of the low-boom demonstrator X-59 [10]. This demonstrator plane aims to perform supersonic cruise at Mach 1.4 with a reduced sonic boom, trying to achieve a level on Stevens' MkVII Perceived Level of Noise metric [11] of 75 dB or lower. This level would mean a significant reduction compared to the sonic boom level of above 100 dB for conventional supersonic airliners. Through this configuration [12], NASA tries to assess the level of annoyance of low-boom supersonic aircraft, and to help regulators define new limits and metrics for sonic booms [13].

The simulation approach for the evaluation of the sonic boom noise on the ground follows the scheme of Figure 1: computation of the sonic boom generation in the zone near the aircraft, then propagation of the pressure disturbance through the atmosphere up to the ground.

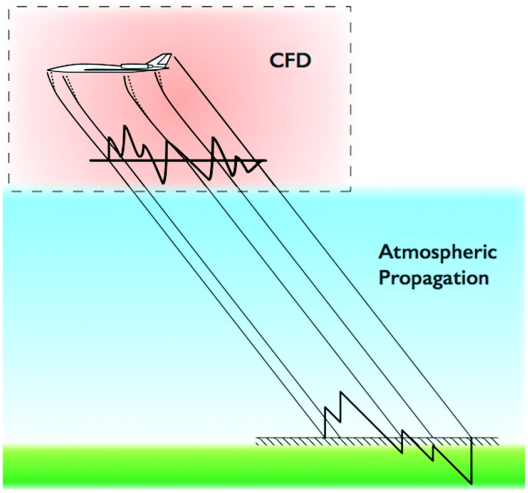

Figure 1. Schematic view of the near-field and far-field domain for sonic boom simulation.

The near-field domain is the region in the vicinity of the aircraft where shock formation occurs and where non-linear phenomena are strong, including shock–shock interactions, shock bending, and cross-flow. The near-field region is usually evaluated using Computational Fluid Dynamics (CFD) with various numerical techniques. Alternatively, wind tunnel measurements can provide insight into the shock waves generated by a fuselage.

For the subsequent far-field modelling, the resulting pressure distribution from the near-field simulation would be used as an input. In this domain, the impact of atmospheric variations and sound absorption is modelled. Due to this dependency, the accuracy of the sonic boom prediction relies on the soundness of the near-field simulations and its signatures.

Nevertheless, other methodologies were studied for the simulation of sonic booms by using CFD to compute the shock waves from reference altitude to the ground, in the far-field domain. For example, Yamashita and Suzuki [14] studied the sonic boom signature on the ground by using just a single CFD domain, which spans from the cruising altitude to the ground instead of using nonlinear equations for the far-field propagation [15]. Those results were in good agreement with flight test data.

Another methodology used for the near-field prediction of sonic booms is utilizing CFD with a Multi-Block structured grid code developed by Jaxa with Euler equations and considering jet-on effects [16]. In their work, the convection terms of the governing

equations are discretized using the AUSMDV scheme with MUSCL extrapolation and min-mod limiter.

Wintzer and Kroo used an adjoint-driven mesh refinement that allows for the rapid and automated generation of volume grids to study the near-field domain of a low-boom configuration [17].

Emmanuelli et al. have studied sonic boom propagation over real topography, and the full two-dimensional Euler equations are solved using finite-difference time-domain techniques [18]. A similar application was suggested by Dragna that studied the sonic boom reflection over urban areas using numerical simulations based on the Euler equations analyzing a classical N-wave and a low-boom wave [19].

Since 2014, NASA has been promoting the AIAA Sonic Boom Prediction workshop, which aims to define numerical methodologies to predict sonic booms from generation to propagation [20–22]. The cross-validated methodologies and results of the workshop's participants represent the state-of-the-art in the prediction of sonic booms in the near-field region of an aircraft.

Previous studies [23] explored the validation of the approaches suggested in the Sonic Boom Workshop, while this work focuses on applying the numerical procedure to novel aircraft layouts, ranging in speed from low supersonic to Mach 5. The aircraft concepts were extracted from the configurations proposed in the European project H2020 MORE&LESS [24].

Figure 2 displays the analyzed configurations. On the left is a Mach 2 "Concorde-like" configuration with biofuel as propellant (CS1, Case Study 1), and on the right is a Mach 5 scramjet civil aircraft fueled with liquid hydrogen (CS3, Case Study 3). The latter was derived from the Mach 8 vehicle of the STRATOFLY project [25–27].

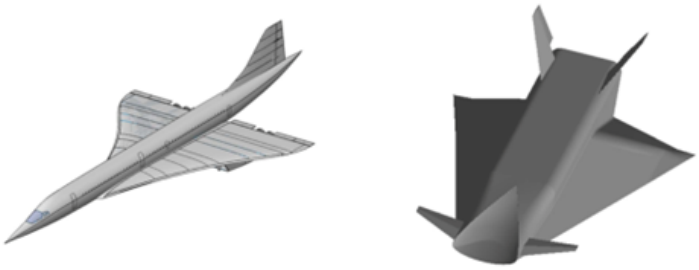

Figure 2. CAD geometries: CS1 (Mach 2) on the left and CS3 (Mach 5) on the right.

For both configurations, sonic boom is computed for several operating conditions. A detailed analysis of the noise field around the aircraft is carried out, like the evaluation of effect of altitude and Mach variations on the pressure field. The numerical approach adopted for the test cases of this paper is introduced in Section 2, together with the physical models for the simulations and the case conditions. Particular attention is devoted to the setup of computation domains, highlighting the procedure for the grid generation and the constraints for obtaining accurate grids. Section 3 presents and discusses the simulation results, emphasizing the peculiarities of the analyzed case studies. Finally, Section 4 is presented and ideas for future development are discussed.

2. Methodology

CFD techniques are used to study the flow around a supersonic aircraft due to the strong non-linearities and three-dimensional interactions near the fuselage. In the vicinity of the aircraft, the aerodynamic effects dominate over the refraction effects of an inhomogeneous atmosphere, which would gain relevance in a subsequent far-field propagation of the sonic boom.

While details on the far-field modelling for a full sonic boom simulation can be found in papers dedicated to the topic [28,29], the object of this work is the near-field computation of sonic booms.

Over the past decade, the study by CFD of sonic boom prediction has undergone numerous improvements [30]. After previous validation work [23], we selected two computational solvers to evaluate the pressure field around the aircraft in supersonic condition, applying the recommendations and improvements found in the literature and early results.

2.1. CFD Approach

Near-field CFD simulations are conducted utilizing both the commercial Ansys Fluent [31] 2022 R1 code and the open-source SU2 [32] code. These codes employ an unstructured finite-volume approach to solve the Reynolds-Averaged Navier–Stokes (RANS) equations, with gradients computed using a Green–Gauss method. In Fluent, a convergence strategy employing an adaptive CFL number is utilized, while SU2 employs a fixed CFL value to control numerical oscillations arising from CFL relaxation in central schemes. All simulations are carried out without turbulence models, solving inviscid Euler equations with an ideal gas model for the air phase. Literature results related to sonic booms highlight the possibility of using Euler equations to simulate the shock waves produced by a supersonic configuration [23,33–35], without loss of accuracy due to not taking into account the boundary layer presence.

Considerable effort is dedicated to exploring various numerical schemes to identify the most suitable one for sonic boom generation [23]. Numerical schemes play a crucial role in translating equations from continuous models to discrete models implemented in computational solvers. For the supersonic Mach numbers studied here, Fluent offers the second-order upwind implicit ROE [36] scheme with Flux-Difference Splitting [37] (ROE-FDS), based on the Roe scheme, which approximates a Riemann solver. ROE-FDS splits fluxes consistently with their corresponding flux method eigenvalues, particularly useful for capturing discontinuities like shocks.

Also, the advection upstream splitting method (AUSM) has been used in the literature for sonic boom evaluation [38–40]. The scheme's core lies in breaking down the flux vector into convective and pressure components. This division ensures that AUSM accurately captures shock discontinuities without introducing unwanted numerical artifacts. By employing an upwinding strategy, the method calculates fluxes at cell interfaces, ensuring accurate information transfer across the computational domain. Unlike fixed flux-splitting coefficients used in other methods, AUSM dynamically adjusts these coefficients based on local flow conditions, guaranteeing stability and accuracy across various flow regimes. Additionally, it incorporates a flux-difference splitting approach, improving accuracy near discontinuities by considering both convective and pressure gradient terms comprehensively.

In SU2, besides the ROE scheme without FDS modification, several other numerical schemes are available. After several tests [23], the HLLC numerical scheme was chosen. The particular scheme introduced by Toro modifies the HLL scheme to restore missing contact and shear waves in the Euler equations. The HLLC scheme enables capturing the effects of velocity discontinuities in the transverse direction without adding unnecessary diffusion in regions, which have been already characterized by turbulent diffusion in the horizontal plane.

2.2. Computational Domain

The definition of the mesh strategies, in terms of refinement and adaptation approach, allows us to properly track discontinuities, but this requires specific effort. In this paper, the topology of the computational grid follows a hybrid approach. The computational mesh is composed of two different parts: an unstructured zone around the aircraft geometry, and a structured zone in the remaining part of the domain.The unstructured part is designed as a half cylinder, while the structured part is designed using a blocking technique and it is aligned with the cone Mach angle μ, as in Figure 3. The numerical elements are hexahedral in the structured domain, tetrahedral in the unstructured zone, and pyramidal to connect the two zones, and the number of cells for both configurations are above 20 million. The

number is 21.5 for CS1,while for CS3, two different refinements were investigated; the coarser one has 25 million elements, while the finer one has 37.

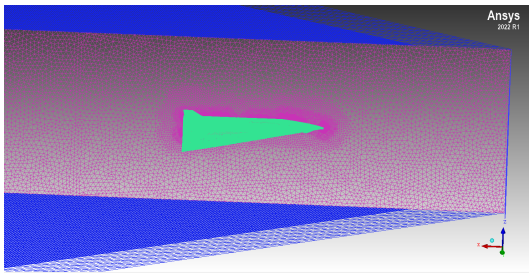

Figure 3. Hybrid grid approach: inner unstructured mesh (pink) and outer structured inclined mesh (blue).

Compared with a full unstructured or full structured mesh approach, the mixed-grid strategy has the advantage of preserving accuracy as well as efficiency.

This hybrid approach has been validated by NASA through the Sonic Boom Prediction Workshop, as testified in [20–22].

Previous work has highlighted the importance of having a good alignment in the grid [41]. In particular, for high displacement in the z direction, differences in the signature for small misaligned grids were visible. As reported in [42], Cartesian meshes can be effective in out-of-body signature computation as long as the mesh is nearly aligned with the Mach μ angle of the free flow. Good alignment reduces dissipative effects and the number of elements, such that signatures can be computed for distances up to $H/L = 5$ without having an extremely high computational cost.

The H/L ratio is defined as the radial distance in relation to the aircraft's characteristic body length, such that $H/L = 3$ describes a radial distance of 3 body lengths. In our study, 3 times the aircraft's body length means a radial distance of $H = 185$ meters for CS1, and $H = 225$ meters for CS3. Pressure signatures are extracted from the CFD solution at those radial distances.

A grid in perfect alignment to the Mach angle could cause the sonic glitch phenomenon, which is avoided by introducing a very small misalignment $\mu \pm \theta$, with $\theta \ll \mu$ [43].

2.3. CS1 Test Case

The first geometry analyzed was a modified version of the Concorde aircraft, shown in Figure 4, able to fly at Mach 2 using biofuel as the propellant [44]. The design process starts from a set of design and operational requirements very similar to the reference Concorde aircraft:

- Range $\geq$ 7200 km;
- Passengers $\geq$ 120;
- MTOW $\leq$ 200,000 kg;
- Cruise @ Mach 2.

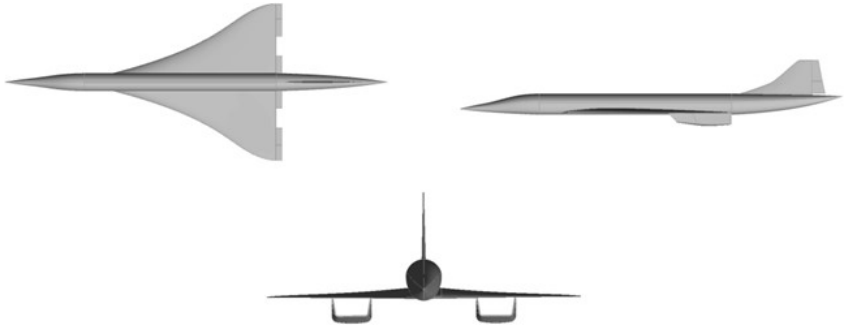

Figure 4. CS1 reference aircraft, 3 views.

In terms of geometrical configuration, the CS1 vehicle has a classical aeronautical shape with the characteristics of Table 1.

Table 1. CS1 geometric and performance data.

Characteristic	Value
Design GTO Mass [kg]	179,849
OEW [kg]	79,460
Design fuel weight [kg]	85,289
Design Payload weight	15,200
Wing Surface [m^2]	358
Aircraft Length [m]	61.7
Wingspan [m]	25.6
Design Range [km]	6500
Cruise Altitude [m]	18,000
Thrust to weight ratio (dry at TO)	0.4
Wing Loading [kg/m^2]	494
Lift over drag ratio	7
Max Mach	2.2
Required Runway Length [m]	3400

Aerodynamic and propulsive databases [45] are the basis of the definition of a reference mission. Figure 5 reports the mission profile with the variation of the aircraft altitude, with the relative angle of attack variation during flight. Specific points of the supersonic flight phases are identified as the reference operative condition for the estimation of sonic boom annoyance, as reported in Table 2.

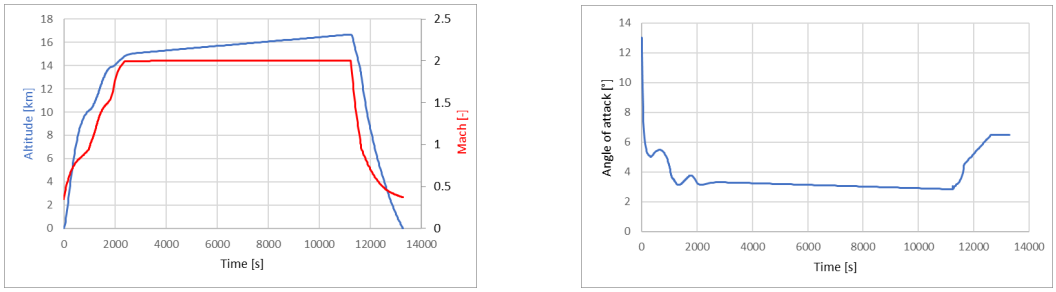

Figure 5. CS1 mission profile and angle of attack variation.

Table 2. CS1 simulation parameters.

Operating Conditions	Mission Point 1	Mission Point 2	Mission Point 3
Mach number	1.5	1.5	2.0
Angle of attack [deg]	4.0	4.5	3.5
Altitude [m]	17,500	15,000	18,500
Pressure [Pa]	8120.51	12,044.6	6935.86
Temperature [K]	216.6	216.6	216.6

Computational Grid

The hybrid grid approach requires the creation of two computational domains, an inner domain around the aircraft and an outer domain up to the far-field. The inner domain can be produced with computational cells of any type, with structured or unstructured behavior, with the aim to better simulate the aerodynamic flow near the vehicle. The outer domain has to follow the Mach lines, which identify the directions of the shock waves, and consequently, the most accurate approach is to create a structured grid with the desired inclination. The results of this work for the CS1 test case can be seen in Figure 6; the overall

shape of the mesh grid highlights the expected direction of the Mach lines, while in the left zone of the figure, it is possible to notice the difference in the meshing approach in the inner zone (unstructured grid) compared to the outer zone (structured grid).

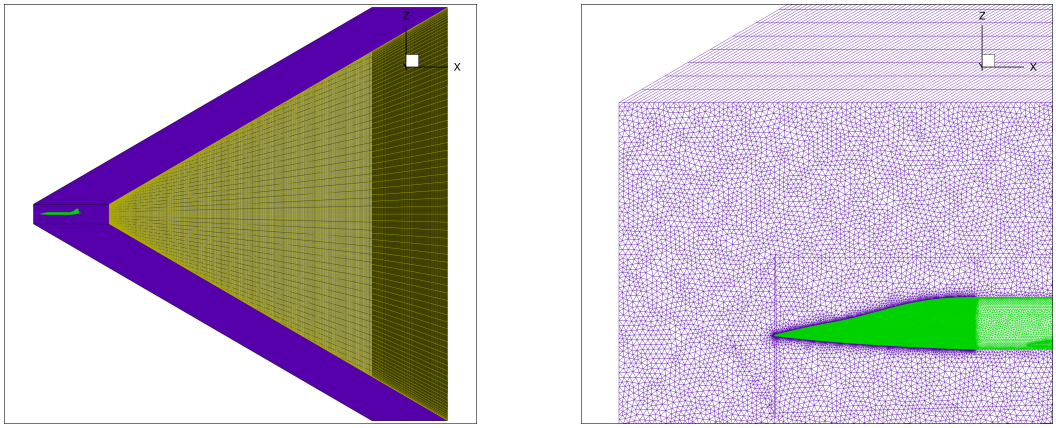

Figure 6. CS1 computational grid, overall grid domain (**left**), and particular cells around the aircraft (**right**).

The number of cells in the complete domain is approximately 21.5 million, while for a low-fidelity aerodynamic grid, it is about 2.1 million elements for the same configuration [45]. The goal of the simulations presented in this work is to propagate the pressure variations of the shock waves produced by the aircraft in the whole computational domain, avoiding numerical artifacts like artificial dissipation. The differences between an aerodynamic simulation and an aeroacoustic computation are pointed out in Figure 7, where the flow fields evaluated using those two different approaches are compared. While the aerodynamic solution leads to good results in terms of global coefficients, lift and drag values agree with the reference values [45], and the pressure flow field is completely different from the aircraft. The pressure variations are dissipated by the computational grid used in the aerodynamic simulation, while they are perfectly visible in the aeroacoustic simulation up to the far-field of the domain.

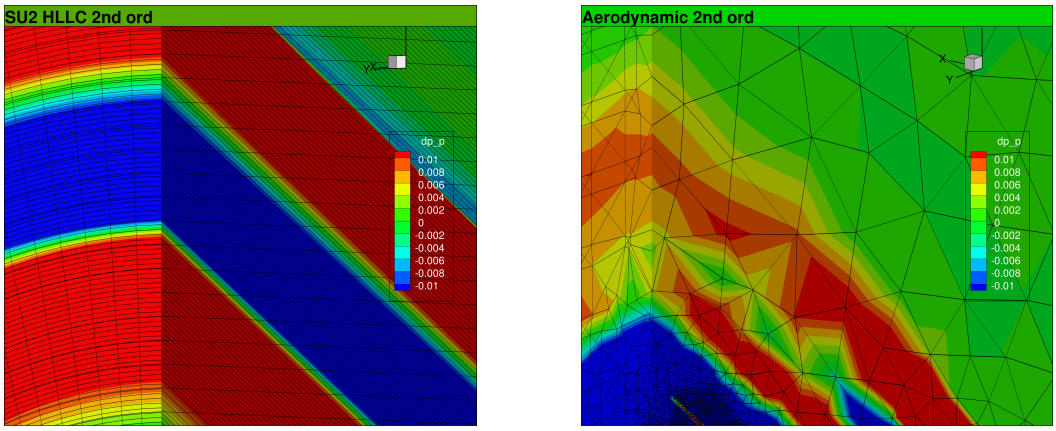

Figure 7. CS1 mesh grid, comparison between aeroacoustic (**left**) and aerodynamic (**right**) mesh construction approaches.

2.4. CS3 Test Case

Starting from the aircraft developed during the H2020 STRATOFLY project [25–27], a modified version at the conceptual design level was evaluated to increase efficiency and sustainability by operating at lower altitudes and Mach numbers.

The STRATOFLY aircraft was capable of flying at Mach 8 at an altitude of about 35 km, having a 94 m long configuration and an MTOW of about 400,000 kg with 180 tonnes of

LH_2, while the CS3 aircraft concept flies at a Mach number of 5 and altitude of about 31 km. The CS3 geometry was derived from the STRATOFLY concept by adopting a scaling law along the x-axis of 0.80, and the overall length is 75.16 m; the result is visible in Figure 8, while additional characteristics of the aircraft are available in Table 3.

The CS3 configuration is a waverider aircraft with engines and air duct integrated within the airframe, allowing for the maximization of lift generation without introducing additional drag penalties. Previous studies [46,47] investigated the aerodynamic behavior of this typology of configuration in the hypersonic regime.

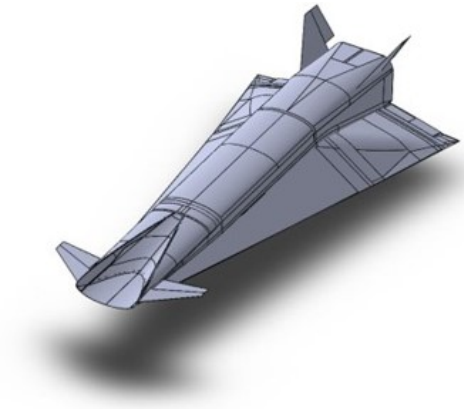

Figure 8. CS3 reference aircraft.

Table 3. CS3 main characteristics.

Characteristic	Value
Overall length [m]	75.16
Wingspan [m]	41.0
Reference lifting surface [m^2]	2000
Internal Volume Arrangement [m^3]	8000
Available fuel volume [m^3]	1582
Payload capacity [kg]	26,400
Reference Range [km]	19,000
MTOW [kg]	288,400
OEW [kg]	150,000
Available fuel mass [kg]	112,000

An aerodynamic database of the aircraft and an associated propulsion database were evaluated to define a realistic mission profile of the aircraft and to validate the case study [48]. For the aerodynamic database, lift and drag coefficients were found by running a different CFD simulation. This separate study used an unstructured grid on a halved CAD model by leveraging the ANSYS-ICEMCFD grid generator and the ANSYS Fluent 2021 R2 solver. The mission profile for the configuration shows that it can complete long-haul missions, reaching Mach 5 during the cruise phase at altitudes of about 30,000 m while carrying 200 passengers onboard, as shown in Figure 9.

Comparing the mission profiles of CS1 and CS3 test cases, we can highlight the differences between them. CS3 is a waverider aircraft that requires a small variation of the angle of attack during flight, a very high Mach number, and a higher flight altitude than CS1's operating conditions.

Based on the operating conditions of Figure 9, a test matrix for the numerical simulations was chosen for the CS3 aircraft and is reported in Table 4. In addition, a test point of 28.0 km altitude was evaluated to highlight the difference in the pressure signature due to altitude, and consequently different free-stream static pressure.

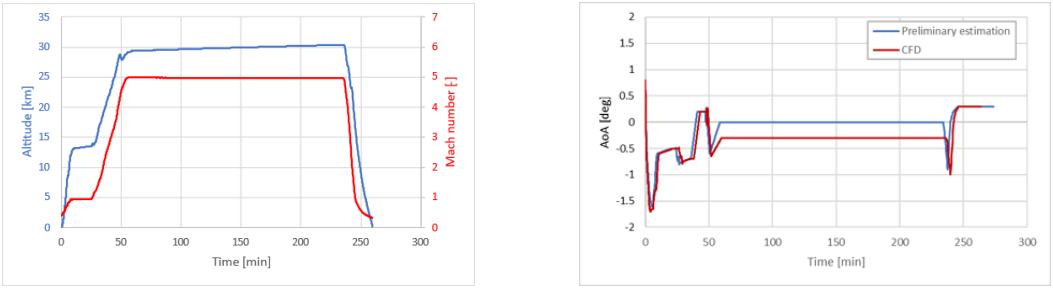

Figure 9. CS3 mission profile and angle of attack variation.

Table 4. CS3 simulation parameters.

Mach Number	Altitude [km]	Pressure [Pa]	Temperature [K]	Mission Point
4.0	31.0	1008.23	227.650	1
4.2	31.0	1008.23	227.650	2
4.4	31.0	1008.23	227.650	3
4.6	31.0	1008.23	227.650	4
4.8	31.0	1008.23	227.650	5
5.0	31.0	1008.23	227.650	6
5.0	28.0	1586.29	224.650	7

Computational Grid

To analyze the aeroacoustic performances of the CS3 aircraft, several computational grids with different refinements were produced in order to improve the quality of the results. In order to reduce the computational cost of the simulations, just half of the vehicle was considered in the simulations due to its symmetric shape, and the computational domain can be seen in Figure 10. Since the simulations cover different Mach numbers, a detailed structured grid for every Mach number shall be constructed and resolved. The grid is not perfectly aligned with the Mach angle μ in order to avoid the Sonic Glitch phenomenon. In particular, the misalignment angle θ in the structured grid was selected as 0.3°, as suggested by Anderson [42].

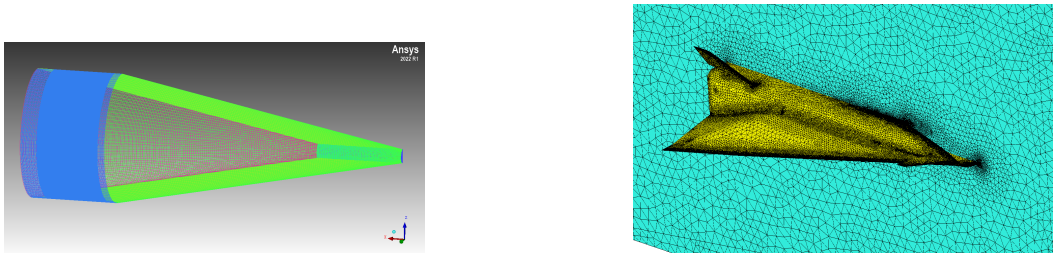

Figure 10. CS3 computational domain (**left**) and detail of the mesh grid around the aircraft (**right**).

To capture shock waves effectively in high-Mach-number simulations, the computational domain has dimensions of one body length in front of the aircraft, and five body lengths after the geometry. The number of elements in the unstructured inner mesh totals 14 million for the coarser grid and 25 for the finer one. As expected, the finest grid has a number of elements that is higher compared to the CS1 configuration, which is due to the dimensions of the geometry. The external structured mesh has 10 to 12 million elements, depending on the Mach number considered; a higher Mach number requires a higher number of elements. For the aspect ratio of the computational elements, the literature shows that an aspect ratio between 2 and 4, for all the directions except for the direction normal to the Mach wave, improves the cost-to-accuracy ratio [49]. During the Second Sonic Boom Prediction Workshop, an extensive study regarding the aspect ratio was conducted [21], indicating that a higher aspect ratio worsens aerodynamics coefficients. So while higher

aspect ratios reduce the number of cells required for a given test case, they increase the order of uncertainty. For the CS3 case study, the maximum aspect ratio is 4.5.

2.5. Solver Setup

For this work, open-source SU2 Multiphysics Simulation and Design Software version 7.2.0 and the commercial ANSYS FLUENT 2022 R1 software are used for the CS1 and CS3 simulations, respectively.

Both softwares include several numerical schemes, turbulence models, and boundary conditions to cover different fluid-dynamic problems. The near-field sonic boom simulation was solved using an Euler approach without turbulence model activation.

In the CS1 test case, SU2 with an HLLC numerical scheme was adopted [23]. The numerical gradients are computed using a Green–Gauss approach. The CFL number is fixed to a unitary value. Two upwind numerical schemes were used for the CS3 case study: a Roe-FDS and an advection upstream splitting method (AUSM).

The Roe numerical scheme solves hyperbolic conservation laws for CFD. Unlike traditional upwind schemes, it incorporates approximate Riemann solvers at each cell interface with the objective of capturing the wave structure and resolving discontinuities. The method transforms the governing equations into a more manageable form, facilitating efficient numerical integration. The Roe scheme's primary breakthrough lies in its adept handling of non-linearities and varying flow conditions.

On the other hand, the AUSM numerical scheme computes fluxes across cells, providing accurate information transfer and evaluation of strong shocks and abrupt changes. It also includes a flux-difference splitting computation method, improving resolution of discontinuities and taking into account pressure and convective variation terms.

3. Results

The pressure signature is usually evaluated at a distance from the aircraft that is proportional to the length of the vehicle itself. Named L, the length of the airplane, the pressure variation is extracted from the flow field at a radial distance H following the formulation $H/L = 1$, $H/L = 3$, and $H/L = 5$. Generally, the main distance is three aircraft lengths, and it is used because it allows a proper evaluation of the pressure signature.

In addition, to better analyze the effect of the shape of the vehicle on the shock wave generation, the pressure signature is evaluated at different azimuth angles around the aircraft, as shown in Figure 11. The position at a 0-degree azimuth angle is below the configuration, the position at 90 degrees is the position along the axis of the wing, while the position at a 180-degree radial angle is above the aircraft.

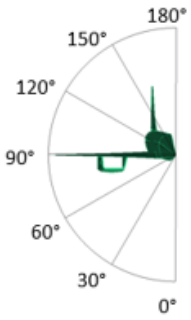

Figure 11. Azimuth angles for pressure extraction around an aircraft.

3.1. CS1 Noise Performances

The noise performance evaluation of CS1 aircraft, in the operating conditions of Table 1, shows the capability of the computational approach explained in the previous paragraphs.

The pressure variation in the aeroacoustic problems is usually evaluated with the following formulation:

$$dp/p = \frac{p_s - p_0}{p_0} \quad (1)$$

In Equation (1), p_0 is the free-stream static pressure and p_s is the one extracted at a specific height-to-length H/L location.

The shock waves around the CS1 configuration are clearly visible in Figure 12 for mission point 1, where the Mach number variations are highlighted. As expected from the shape of the aircraft, the aerodynamic field under the CS1 is different from the flow field above the vehicle. The pressure signature estimated at the position $H/L = 3$ is shown in Figure 13. The typical N-wave shape of the pressure variation is well simulated, with a good definition. It is possible to notice a small pressure peak before the N-wave; this is due to the shock wave starting from the nose of the aircraft, and it interacts with the shock waves starting from the wing, consistent with the physics of the problem.

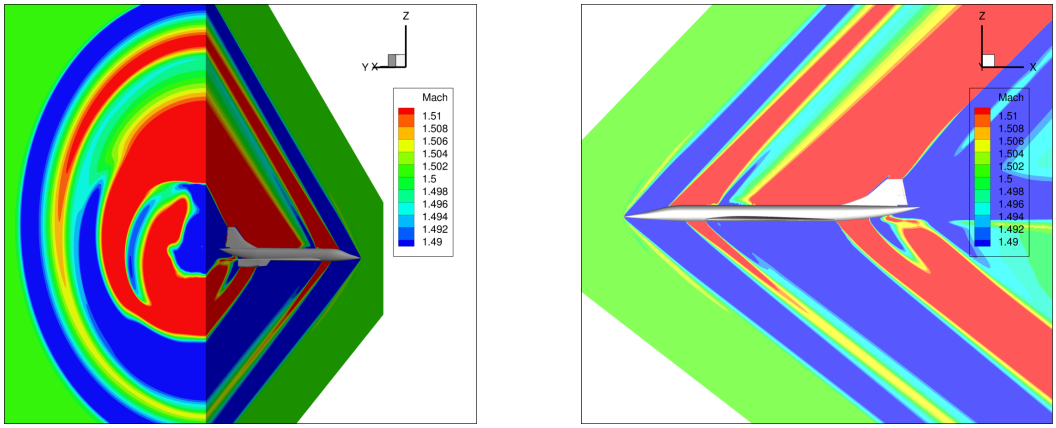

Figure 12. CS1 mach number field for mission point 1, Mach 1.5, AoA 4.0, altitude 17,500 m.

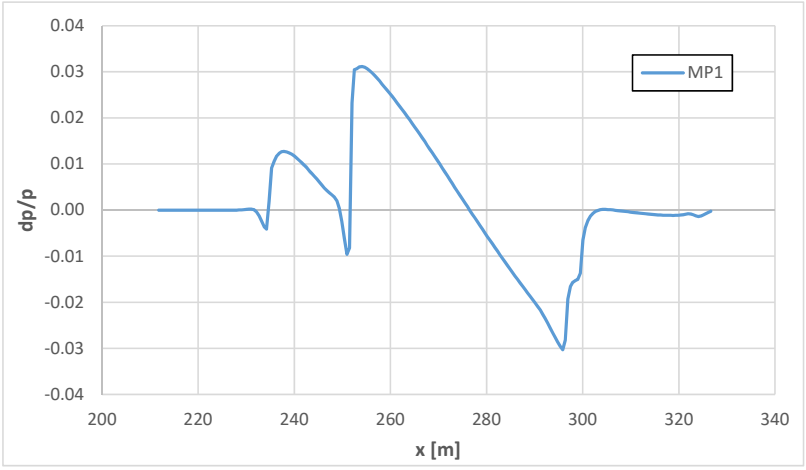

Figure 13. CS1 pressure signature at $H/L = 3$ for mission point 1.

Following the procedure described at the beginning of the section, the pressure signature in the radial direction around the CS1 geometry, at angles from 0 degrees (under the aircraft) to 180 degrees (above the aircraft), was extracted. In left picture of Figure 14, pressure signature for angles up to 40 degrees are compared, pointing out the variation of N-waves in the zone of influence of the wing. Moreover, it can be noticed that the greatest value of each pressure distribution decreases when moving from under the aircraft to the lateral part where wings are located. In the right picture of Figure 14, the

noise performance of the CS1 configuration is shown in decibels for each radial position from 0 to 180 degrees, at different distances from the aircraft. From the position close to the configuration $H/L = 1$, the noise values decrease to the position far from the CS1 $H/L = 5$. It is possible to notice that below the aircraft, the noise peaks are higher than the other positions.

Mission point 2 results are shown in the Figures 15 and 16. In this operating condition, the Mach number has the same value of mission point 1, while the reference pressure is higher. The effect of reference pressure is to increase the values of peaks in the pressure signature, as confirmed by comparing Figures 13 and 16.

This behavior becomes clearer in the right picture of Figure 17, where the value of noise in decibels in the position 0 degrees (under the aircraft) is higher than 150 dB, which was the value in the same position in the condition of mission point 1, as shown in Figure 17.

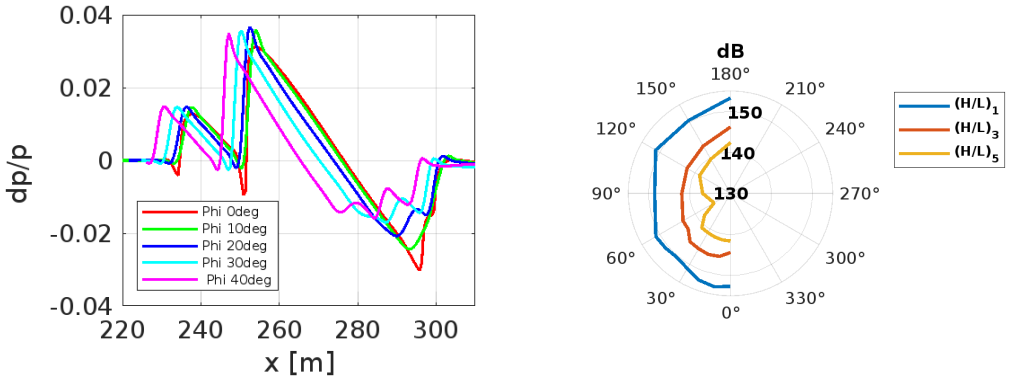

Figure 14. CS1 pressure signature in radial position around the aircraft at $H/L = 3$ on the left, values in dB on the right, for mission point 1.

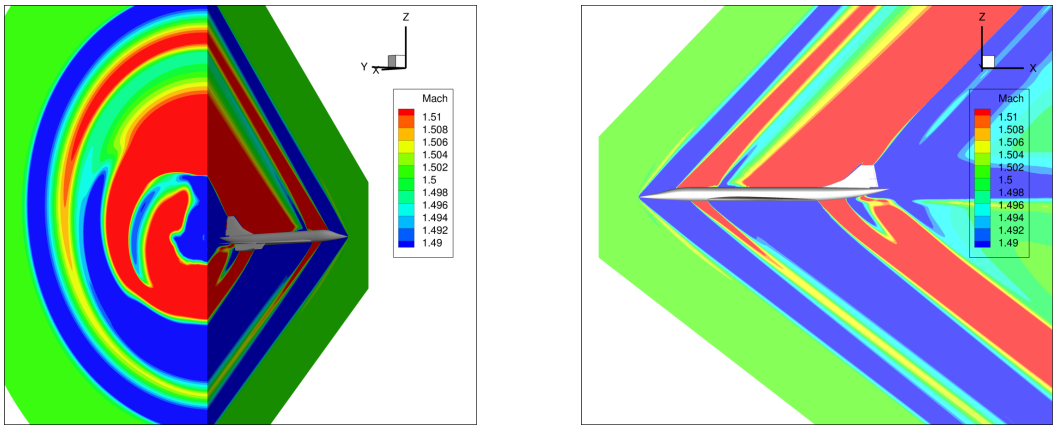

Figure 15. CS1 mach number field for mission point 2, Mach 1.5, AoA 4.5, altitude 15,000 m.

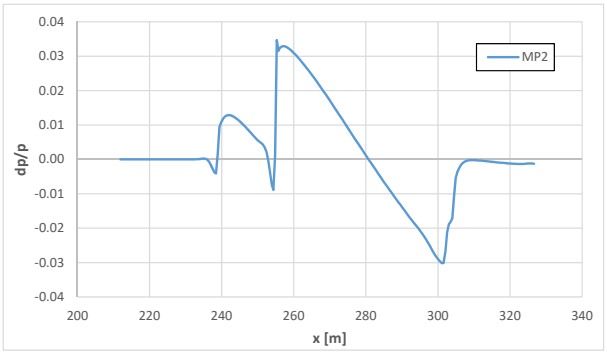

Figure 16. CS1 pressure signature at $H/L = 3$ for mission point 2.

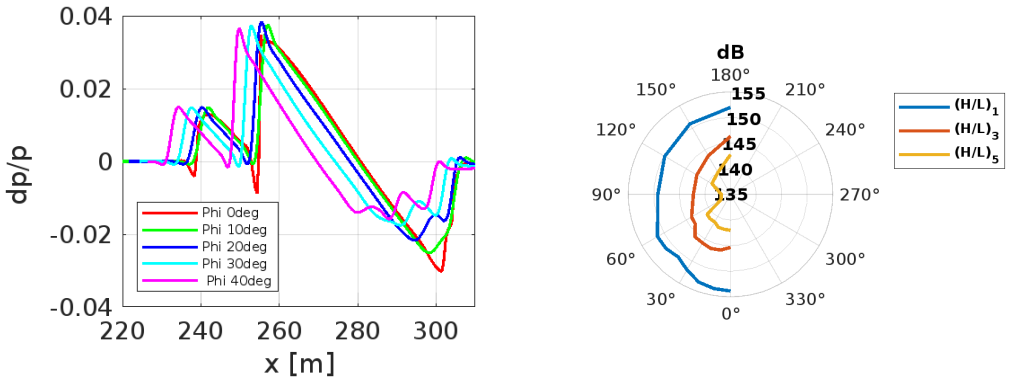

Figure 17. CS1 pressure signature in radial position around the aircraft at $H/L = 3$ on the left, values in dB on the right, for mission point 2.

The last results related to mission point 3 are in Figures 18 and 19. Mach number in this case is higher than the mission point 1 value, while the reference pressure has a lower value. The effect of the Mach number is to modify the extension of the N-wave, as confirmed by comparing Figures 12 and 18, with a noticeable difference also in maximum and minimum values. The results of Figure 20 confirm the good performance of the procedure implemented to evaluate the sonic boom generation near the aircraft.

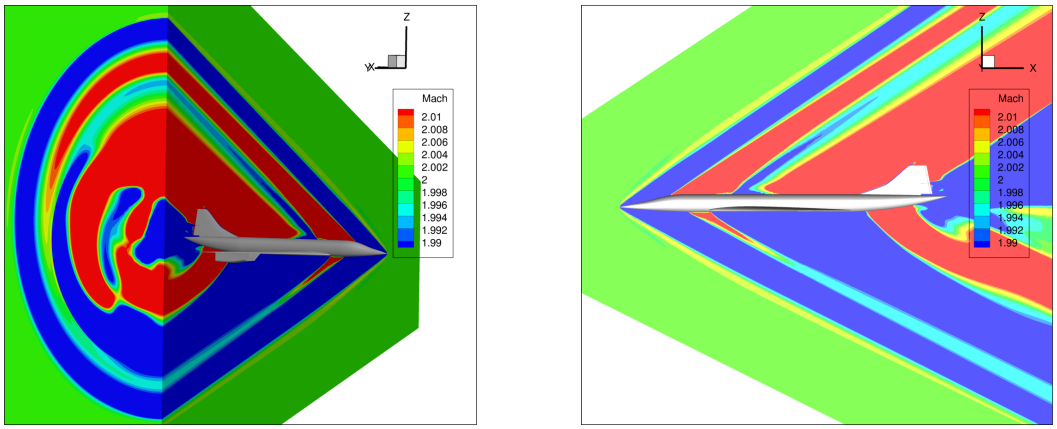

Figure 18. CS1 mach number field for mission point 3.

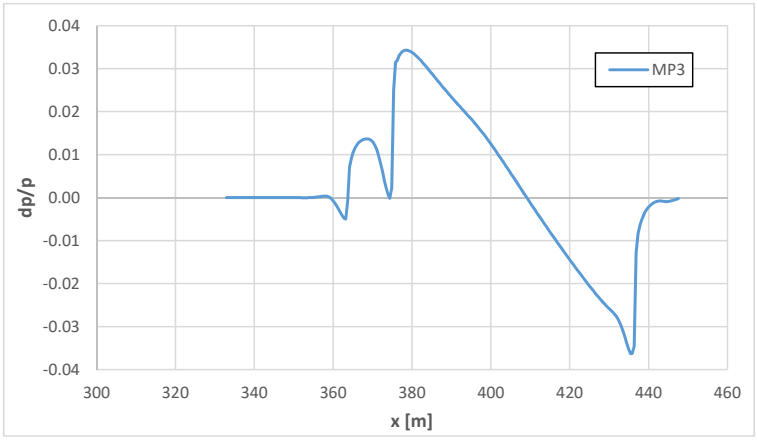

Figure 19. CS1 pressure signature at $H/L = 3$ for mission point 3, Mach 2.0, AoA 3.5, altitude 18,500 m.

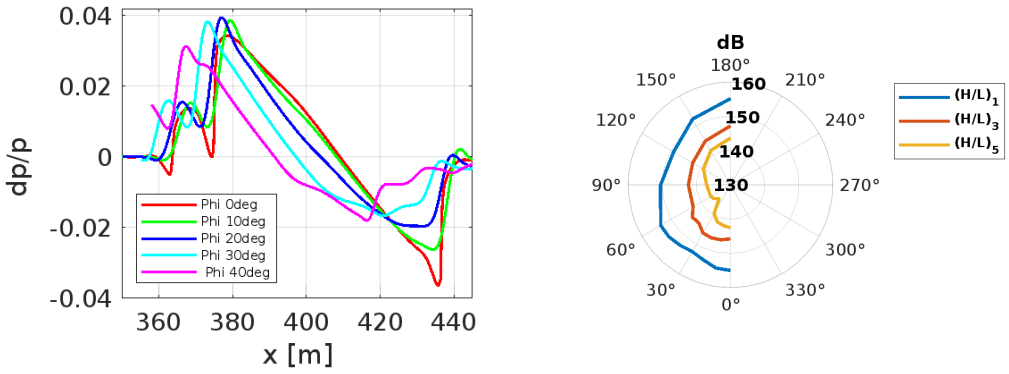

Figure 20. CS1 pressure signature in radial position around the aircraft at $H/L = 3$ on the left, values in dB on the right, for mission point 3.

3.2. CS3 Noise Performances

To characterize the CS3 case study, a wide range of Mach numbers and the exploitation of different grids were considered while keeping constant the angle of attack due to the mission profile in Figure 9.

Pressure and Mach number distribution around the aircraft geometry show the existing shock wave, as highlighted in Figure 21. As expected from the shape of the configuration, the aerodynamic field under the aircraft is different than the field above it, as highlighted in the pictures in Figure 21.

The results plotted in Figure 21 were obtained for the reference flight condition of the aircraft, which was mission point 6 of Table 4, with Mach number equal to 5, an altitude of 31 km, and a 0-degree angle of attack.

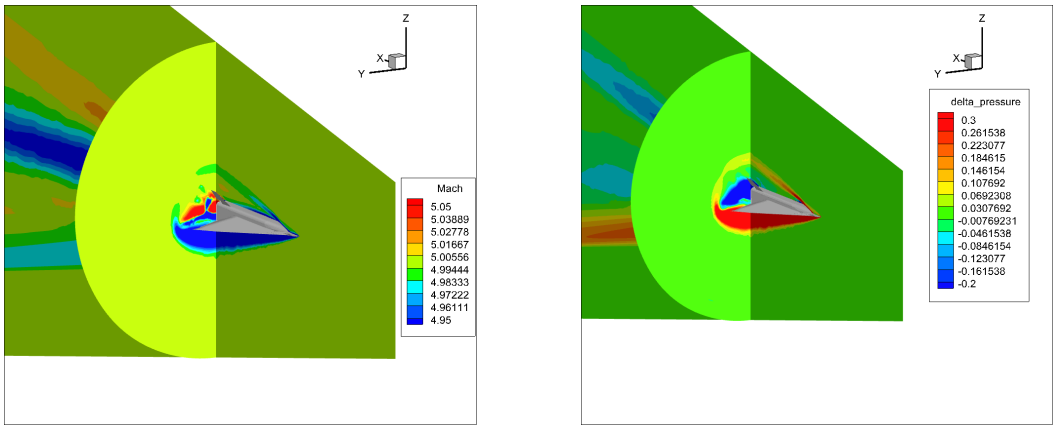

Figure 21. CS3 Mach number (**left**) and delta pressure (**right**) contours for mission point 6.

An acoustic radial analysis was carried out for the flight conditions shown in Table 4. This radial analysis is essential for further propagation study, to accurately evaluate the pressure signature that will propagate to the ground.

Figure 22 shows the pressure signature extracted at $H/L = 3$ for different angles of extraction between 0° and 90°. It is possible to evaluate important differences in the peak pressure of the signature by varying the angle of extractions, as confirmed by Figure 21. The shape of the pressure signature is not a complete N-wave due to the particular behavior in the expansion region, and it is due to the difficulty of the AUSM numerical scheme in capturing the rear shock.

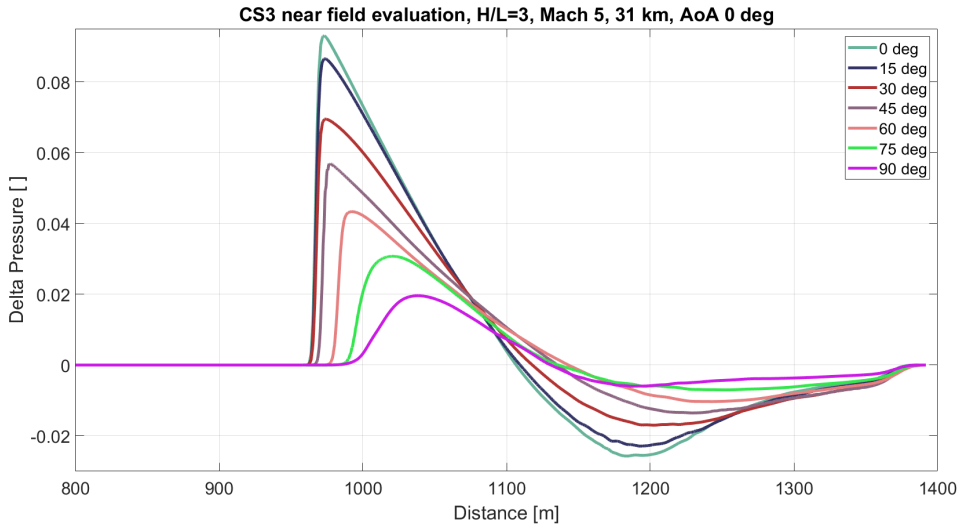

Figure 22. CS3 pressure distribution, radial evaluation at $H/L = 3$.

As can be seen from Figures 22 and 23, there is a substantial difference in the peak pressure signature between the on-track and off-track conditions, and the same behavior was observed for the other Mach numbers. In addition to the difference in radial behavior, there is a strong difference between the peak value in compression and expansion. This is due to the particular geometry of the CS3 configuration, with lifting surfaces starting from the nose of the aircraft and the particular volume distribution.

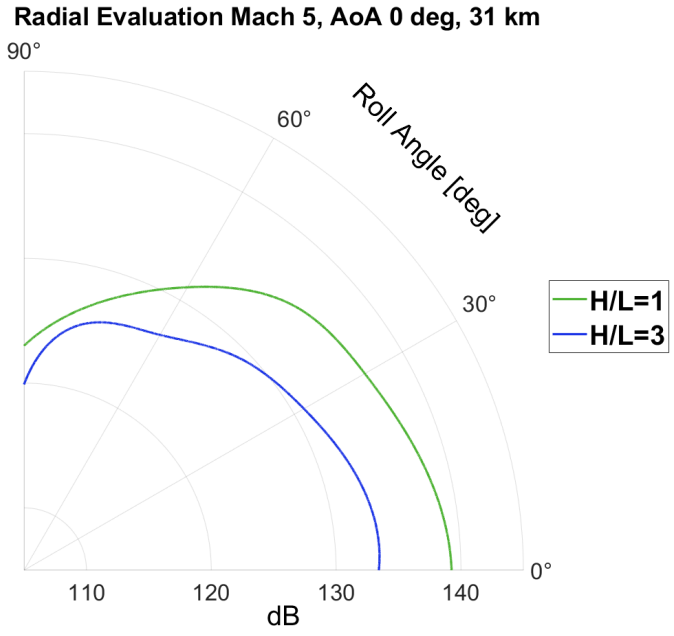

Figure 23. CS3 wave peak pressure levels, radial evaluation at $H/L = 3$.

In order to analyze noise performance in detail throughout the supersonic profile phase, a sensitivity analysis was evaluated by varying the Mach number, as can be seen in Figure 24.

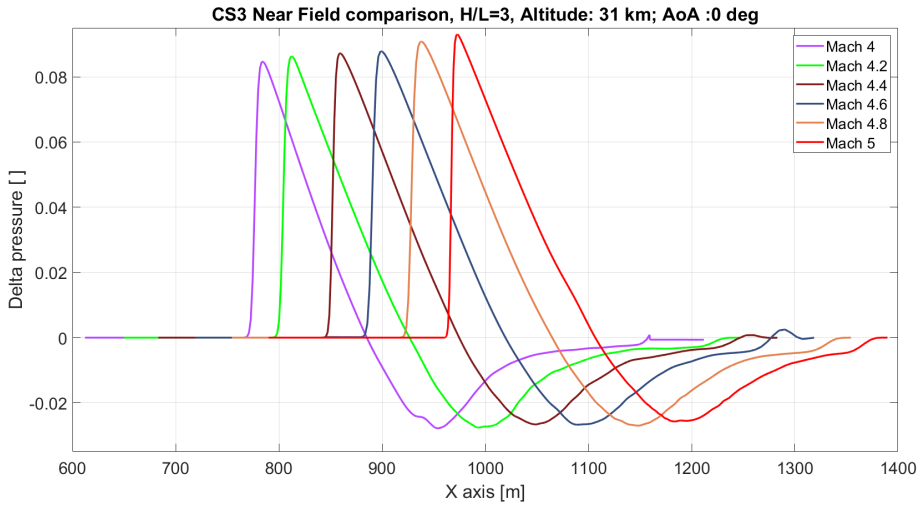

Figure 24. CS3 sonic boom pressure signatures with Mach number sensitivity at $H/L = 3$.

Figure 24 shows the pressure signature for different Mach numbers at distance $H/L = 3$ from the aircraft, and a trend is visible. As expected, there is a small increase in the amplitude of the peak pressure as the Mach number rises; since sonic boom is primarily a function of the shape of the aircraft, and the peak pressure does not increase too much with a small increase in the Mach number.

The sensitivity analysis on Mach number was performed for future investigations in the far-field for trajectory optimization and subsequently identify differences in the ground pressure signature. Additional simulations were made at 28 km altitude and Mach 5, mission point 7 of Table 4, to simulate the beginning of the cruise phase mission, with pressure distributions extracted at $H/L = 3$ and $H/L = 5$. A comparison in the pressure signature at $H/L = 3$ with the end of the cruise point is visible in Figure 25. It is possible to notice that the difference in the pressure signature between the two simulations is almost negligible; at lower altitude, there is a slightly higher peak pressure, and it is coherent with the fact that the aircraft is flying with a higher free-stream static pressure.

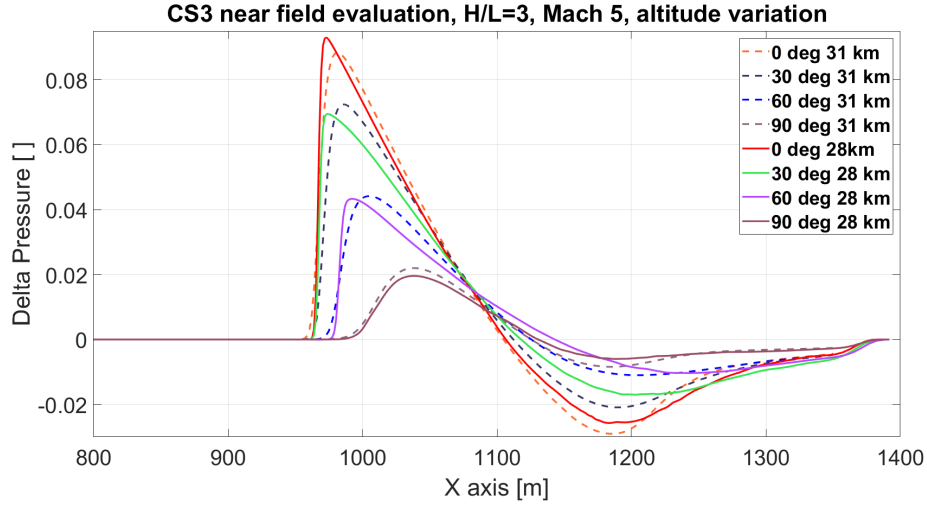

Figure 25. CS3 sonic boom pressure signatures with different altitudes at $H/L = 3$.

Figure 26 reports the extractions made at distance $H/L = 5$ for the beginning of the cruise condition for mission point 7, with Mach 5 and 28 km altitude for different azimuth angles. As for the results at distance $H/L = 3$, the behavior of decreasing peak pressures for increasing azimuth angles is visible.

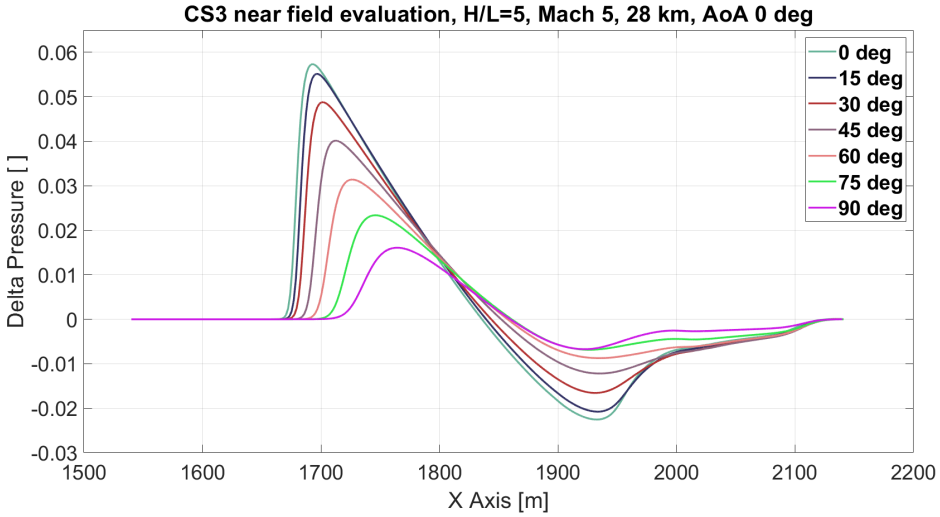

Figure 26. CS3 sonic boom pressure signature at Mach 5, 28 km altitude, $H/L = 5$.

Finally, the impact of different discretization methods is evaluated for mission point 6, and it is reported in Table 5 and Figure 27. The same grid was adopted for the ROE-FDS and AUSM numerical scheme, while a finer grid was evaluated with the AUSM scheme only, in order to highlight possible differences due to grid sensitivity.

In Table 5, the values of lift and drag coefficients are presented and compared with the values computed for the aerodynamic database.

Table 5. Lift and drag coefficients for different schemes and grid sizes.

Scheme	C_L	C_D
AUSM	0.05690	0.01129
ROE-FDs	0.05704	0.01136
AUSM Finer Grid	0.05690	0.01132
Aerodynamic	0.05674	0.01121

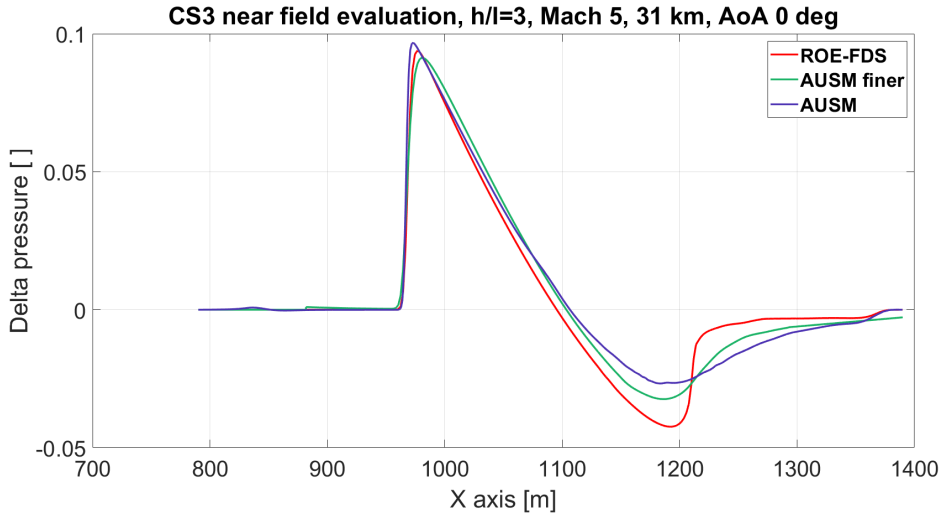

Figure 27. CS3 comparison of pressure signature using different numerical schemes and grid size.

Figure 27 shows that different numerical schemes predict different sonic boom pressure signatures. The positive portion of the signature has a similar behavior and peak pressure for different discretization methods and grid refinement. However, differences are clearly visible in the expansion region between the two numerical schemes. The ROE-FDS scheme predicts the rear shock with a higher magnitude, while AUSM, even with

the finer grid, has difficulties capturing the aft shock. The outcome is that ROE-FDS for this test case is more suitable for the prediction of sonic boom pressure signatures in the near-field.

3.3. Comparison

The two analyzed configurations differ significantly in both geometry and operating conditions. In particular, CS1 has a classic wing and fuselage configuration, while CS3 is a waverider that increases aerodynamic efficiency during the hypersonic cruise phase.

The CS1 shape led to a pressure signature at $H/L = 3$ that is still composed of two bow shocks. This is because the distance between the nose of the aircraft and the wing surface is long enough that these shocks have not yet coalesced. This double shock behavior will be investigated in the far-field with the use of a propagation code to evaluate the pressure signature on the ground. The near-field pressure signature of the CS3 configuration already forms a single strong shock and a linear trend in the expansion region. However, the results obtained with the AUSM discretization method do not have a shape of a typical N-wave.

4. Conclusions

This paper describes a near-field analysis of two innovative supersonic configurations. An open-source code and a commercial code were used to carry out numerical simulations.

The paper reports the procedure adopted to effectively capture the shock waves. An analysis of the differences in the pressure signature for various operating conditions and discretization methods was carried out. For both configurations, the results are in agreement with the physical expectation. For the CS3 waverider model, the simulations have shown a different pressure signature for the off-track condition. Different discretization methods give very different solutions in the aft shock, while for the peak pressure, the differences are negligible.

The results of the CS3 Mach sensitivity analysis show a small increase in the peak pressure amplitude for increasing Mach numbers, while the general shape of the signature remains similar. However, the differences in peak pressure between Mach 4 and Mach 5 for the CS3 configuration are small, which means that the near-field signature has only a small dependency on the Mach number in this speed regime.

The comparison of different cruise altitudes shows small differences in the peak pressure, which are caused by the different free-stream conditions.

In future works, pressure signature results will be propagated on the ground to verify the difference given by mission points and different flight conditions. This will be essential to evaluate the level of annoyance given by different operating conditions and aircraft configurations, to exploit the behavior of a supersonic aircraft.

Author Contributions: Conceptualization R.F., N.V. and J.J.; Methodology S.G., F.P. and A.G.; Formal analysis S.G., F.P. and A.G.; resources S.G., J.J. and F.P.; writing—original draft S.G., F.P. and J.J.; writing—review and editing R.F., N.V. and S.G.; supervision R.F. and N.V. All authors have read and agreed to the published version of the manuscript.

Funding: This research was funded by the European Union's Horizon 2020 research and innovation programme under grant agreement No. 101006856, project MORE&LESS (MDO and Regulations for Low-boom and Environmentally Sustainable Supersonic aviation).

Data Availability Statement: The data presented in this study are available on request from the corresponding author.

Acknowledgments: The authors would like to thank all the partners of the MORE&LESS project.

Conflicts of Interest: The authors declare no conflicts of interest. The results, opinions, conclusions, etc., presented in this work are those of the authors only.

Abbreviations

The following abbreviations are used in this manuscript:

NASA	National Aeronautics and Space Administration
μ	Mach angle
θ	Misalignment angle
ICAO	International Civil Aviation Organization
MORE&LESS	MDO and REgulations for Low-boom and Environmentally Sustainable Supersonic Aviation
CFD	Computational Fluid Dynamic
ISA	subscript for International Standard Atmosphere
SPL	Sound Pressure Level
PLdb	Perceived Noise Level
a	Speed of sound, m/s
H/L	Height over length ratio for extraction
C_L	Lift coefficient
C_D	Drag coefficient
M	Mach number
p_s	Static Pressure
p_0	Free-stream pressure condition
α	Angle of attack, deg

References

1. Liebhardt, B.; Lütjens, K. An Analysis of the Market Environment for Supersonic Business Jets. In Proceedings of the DLRK Tagungsband 2011: 60. Deutscher Luft- und Raumfahrtkongress, Bremen, Deutschland, 27–29 September 2011.
2. Alkaya, C.; Alex Sam, A.; Pesyridis, A. Conceptual Advanced Transport Aircraft Design Configuration for Sustained Hypersonic Flight. *Aerospace* **2018**, *5*, 91. [CrossRef]
3. Aronstein, D.C.; Schueler, K.L. Two Supersonic Business Aircraft Conceptual Designs With and Without Sonic Boom Constraint. *J. Aircr.* **2005**, *42*, 775–786. [CrossRef]
4. Furukawa, T.; Makino, Y. Conceptual Design and Aerodynamic Optimization of Silent Supersonic Aircraft at JAXA. In Proceedings of the 25th AIAA Applied Aerodynamics Conference, Miami, FL, USA, 25–28 June 2007. [CrossRef]
5. Rötger, T.; Eyers, C.; Fusaro, R. A Review of the Current Regulatory Framework for Supersonic Civil Aircraft: Noise and Emissions Regulations. *Aerospace* **2024**, *11*, 19. [CrossRef]
6. Marulo, F. Aircraft Community Noise: The Revenge of a Neglected Problem. *Aerotec. Missili Spaz.* **2015**, *94*, 184–194. [CrossRef]
7. Maglieri, D.J.; Bobbitt, P.J.; Plotkin, K.J.; Shepherd, K.P.; Coen, P.G.; Richwine, D.M. Sonic Boom: Six Decades of Research. 2014. Available online: https://ntrs.nasa.gov/citations/20150006843 (accessed on 4 March 2024).
8. Sun, Y.; Smith, H. Review and prospect of supersonic business jet design. *Prog. Aerosp. Sci.* **2017**, *90*, 12–38. [CrossRef]
9. Seebass, R. Sonic boom theory. *J. Aircr.* **1969**, *6*, 177–184. [CrossRef]
10. Rathsam, J.; Coen, P.; Loubeau, A.; Ozoroski, L.; Shah, G. Scope and goals of NASA's Quesst Community Test Campaign with the X-59 aircraft. In Proceedings of the 14th ICBEN Congress on Noise as a Public Health Problem, Belgrade, Serbia, 18–22 June 2023.
11. Stevens, S.S. Perceived Level of Noise by Mark VII and Decibels (E). *J. Acoust. Soc. Am.* **1972**, *51*, 575–601. [CrossRef]
12. Doebler, W.; Wilson, S.; Loubeau, A.; Sparrow, V. Five-year simulation study of NASA's X-59 low-boom carpets across the contiguous United States of America. In Proceedings of the eForum Acusticum 2020, Lyon, France, 20–24 April 2020; pp. 1001–1008. [CrossRef]
13. Loubeau, A.; Naka, Y.; Cook, B.G.; Sparrow, V.W.; Morgenstern, J.M. A new evaluation of noise metrics for sonic booms using existing data. *AIP Conf. Proc.* **2015**, *1685*, 090015. [CrossRef]
14. Yamashita, R.; Makino, Y.; Roe, P.L. Fast Full-Field Simulation of Sonic Boom Using a Space Marching Method. *AIAA J.* **2022**, *60*, 4103–4112. [CrossRef]
15. Yamashita, R.; Nikiforakis, N. Three-dimensional full-field simulation of sonic boom emanating from complex geometries over buildings. *Shock Waves* **2023**, *33*, 1–19. [CrossRef]
16. Ishikawa, H.; Makino, Y.; Ito, T.; Kuroda, F. Sonic Boom Prediction Using Multi-Block Structured Grids CFD Code Considering Jet-On Effects. In Proceedings of the 27th AIAA Applied Aerodynamics Conference, San Antonio, TX, USA, 22–25 June 2009. [CrossRef]
17. Wintzer, M.; Kroo, I. Optimization and Adjoint-Based CFD for the Conceptual Design of Low Sonic Boom Aircraft. In Proceedings of the 50th AIAA Aerospace Sciences Meeting including the New Horizons Forum and Aerospace Exposition, Nashville, TN, USA, 9–12 January 2012. [CrossRef]
18. Emmanuelli, A.; Dragna, D.; Ollivier, S.; Blanc-Benon, P. Sonic boom propagation over real topography. *J. Acoust. Soc. Am.* **2023**, *154*, 16–27. [CrossRef]

19. Dragna, D.; Emmanuelli, A.; Ollivier, S.; Blanc-Benon, P. Sonic boom reflection over urban areas. *J. Acoust. Soc. Am.* **2022**, *152* 6, 3323. [CrossRef]
20. Park, M.; Morgenstern, J. Summary and Statistical Analysis of the First AIAA Sonic Boom Prediction Workshop. *J. Aircr.* **2016**, *53*, 578–598. [CrossRef]
21. Park, M.A.; Nemec, M. Nearfield Summary and Statistical Analysis of the Second AIAA Sonic Boom Prediction Workshop. *J. Aircr.* **2019**, *56*, 851–875. [CrossRef]
22. Park, M.A.; Carter, M.B. Nearfield Summary and Analysis of the Third AIAA Sonic Boom Prediction Workshop C608 Low Boom Demonstrator. In Proceedings of the AIAA Scitech 2021 Forum, Virtual Event, 11–15 January 2021. [CrossRef]
23. Glorioso, A.; Petrosino, F.; Aprovitola, A.; Barbarino, M.; Pezzella, G. Sonic Boom generation using open source CFD approach. In Proceedings of the AIAA AVIATION 2023 Forum, San Diego, CA, USA, 12–16 June 2023. [CrossRef]
24. Horizon2020. MDO and REgulations for Low-Boom and Environmentally Sustainable Supersonic Aviation. Grant Agreement ID: 101006856, CORDIS European Community Research Results 2021. Available online: https://cordis.europa.eu/project/id/101006856 (accessed on 29 April 2024).
25. Viola, N.; Fusaro, R.; Ferretto, D.; Gori, O.; Saracoglu, B.; Ispir, A.C.; Schram, C.; Grewe, V.; Plezer, J.F.; Martinez, J.; et al. H2020 STRATOFLY project: From Europe to Australi in less than 3 hours. In Proceedings of the ICAS 2021 the 32nd Congress of the International Council of the Aeronautical Sciences, Shanghai, China, 6–10 September 2021.
26. Viola, N.; Fusaro, R.; Ferretto, D.; Gori, O.; Saracoglu, B.; Ispir, A.C.; Schram, C.; Grewe, V.; Plezer, J.; Martinez, J.; et al. Main Achievements of the H2020 STRATOFLY Project. In *Titolo Volume Non Avvalorato*; European Space Agency: Paris, France, 2022; pp. 1–12.
27. Viola, N.; Fusaro, R.; Saracoglu, B.; Schram, C.; Grewe, V.; Martinez, J.; Marini, M.; Hernandez, S.; Lammers, K.; Vincent, A.; et al. Main challenges and goals of the H2020 STRATOFLY project. *Aerotec. Missili Spaz.* **2021**, *100*, 95–110. [CrossRef]
28. Cleveland, R.O.; Hamilton, M.F.; Blackstock, D.T. Time-domain modeling of finite–amplitude sound in relaxing fluids. *J. Acoust. Soc. Am.* **1996**, *98*, 2865. [CrossRef]
29. Rallabhandi, S.K. Advanced Sonic Boom Prediction Using the Augmented Burgers Equation. *J. Aircr.* **2011**, *48*, 1245–1253. [CrossRef]
30. Park, M.A.; Aftosmis, M.J.; Campbell, R.L.; Carter, M.B.; Cliff, S.E.; Bangert, L.S. Summary of the 2008 NASA Fundamental Aeronautics Program Sonic Boom Prediction Workshop. *J. Aircr.* **2014**, *51*, 987–1001. [CrossRef]
31. Ansys Fluent Fluid Simulation Software. ANSYS, Inc., 2018. Available online: https://www.ansys.com/products/fluids/ansys-fluent (accessed on 29 April 2024).
32. Economon, T.D.; Palacios, F.; Copel, S.R.; Lukaczyk, T.W.; Alonso, J.J. SU2: An Open-Source Suite for Multiphysics Simulation and Design. *AIAA J.* **2016**, *54*, 828–846. [CrossRef]
33. Potapkin, A.; Korotaeva, T.; Moskvichev, D.; Shashkin, A.; Maslov, A.; Silkey, J.; Roos, F. An Advanced Approach for Far-Field Sonic Boom Prediction. In Proceedings of the 47th AIAA Aerospace Sciences Meeting including the New Horizons Forum and Aerospace Exposition, Orlando, FL, USA, 5–8 January 2009.
34. Siclari, M.J.; Darden, C.M. Euler code prediction of near-field to midfield sonic boom pressure signatures. *J. Aircr.* **1993**, *30*, 911–917. [CrossRef]
35. Ozcer, I. Sonic Boom Prediction Using Euler / Full Potential Methodology. In Proceedings of the 45th AIAA Aerospace Sciences Meeting and Exhibit, Reno, NV, USA, 8–11 January 2007. [CrossRef]
36. Roe, P. Approximate Riemann solvers, parameter vectors, and difference schemes. *J. Comput. Phys.* **1981**, *43*, 357–372. [CrossRef]
37. Roe, P.L. Characteristic-Based Schemes for the Euler Equations. *Annu. Rev. Fluid Mech.* **1986**, *18*, 337–365. [CrossRef]
38. Dagrau, F.; Loseille, A.; Din, I.S.E. Computational and Experimental Assessment of Models for the First AIAA Sonic Boom Prediction Workshop Using Adaptive High Fidelity CFD methods. In Proceedings of the 32nd AIAA Applied Aerodynamics Conference, Atlanta, GA, USA, 16–20 June 2014. [CrossRef]
39. Yamashita, R.; Suzuki, K. Full-Field Sonic Boom Simulation in Real Atmosphere. In Proceedings of the 32nd AIAA Applied Aerodynamics Conference, Atlanta, GA, USA, 16–20 June 2014. [CrossRef]
40. Luquet, D.; Marchiano, R.; Coulouvrat, F.; Din, I.S.E.; Loseille, A. Sonic Boom Assessment of a Hypersonic Transport Vehicle with Advanced Numerical Methods. In Proceedings of the 21st AIAA/CEAS Aeroacoustics Conference, Dallas, TX, USA, 22–26 June 2015. [CrossRef]
41. Park, M.A.; Campbell, R.L.; Elmiligui, A.A.; Cliff, S.E.; Nayani, S. Specialized CFD Grid Generation Methods for Near-Field Sonic Boom Prediction. In Proceedings of the 52nd Aerospace Sciences Meeting, National Harbor, MD, USA, 13–17 January 2014. [CrossRef]
42. Anderson, G.R.; Aftosmis, M.J.; Nemec, M. Cart3D Simulations for the Second AIAA Sonic Boom Prediction Workshop. *J. Aircr.* **2019**, *56*, 896–911. [CrossRef]
43. Moschetta, J.M.; Gressier, J. The sonic point glitch problem: A numerical solution. In Proceedings of the Sixteenth International Conference on Numerical Methods in Fluid Dynamics, Arcachon, France, 6–10 July 1998; Bruneau, C.H., Ed.; Springer: Berlin/Heidelberg, Germany, 1998; pp. 403–408.
44. Graziani, S.; Viola, N.; Petrosino, F.; Jäschke, J. Comparison between simplified approach and CFD & Propagation tool for sonic boom estimation. In Proceedings of the AIAA AVIATION 2023 Forum, San Diego, CA, USA, 12–16 June 2023. [CrossRef]

45. Roncioni, P.; Marini, M.; Gori, O.; Fusaro, R.; Viola, N. Aerodatabase Development and Integration and Mission Analysis of a Mach 2 Supersonic Civil Aircraft. *Aerospace* **2024**, *11*, 111. [CrossRef]
46. Pezzella, G.; Viviani, A. Analysis of Subsonic/Hypersonic Aerodynamics of a High-Speed Aircraft. *Aerotec. Missili Spaz.* **2024** . [CrossRef]
47. Viviani, A.; Pezzella, G. Aerodynamic performance analysis of three different vehicle concepts. *Aerotec. Missili Spaz.* **2017**, *96*, 16–31. [CrossRef]
48. Gori, O.; Borio, V.; Viola, N.; Roncioni, P.; Marini, M.; Pepelea, D.; Stoican, M.G. From conceptual to preliminary design: Aerodynamic characterization of MR5 civil high-speed aircraft. In Proceedings of the 25th AIAA International Space Planes and Hypersonic Systems and Technologies Conference, Bengaluru, India, 28 May–1 June 2023. [CrossRef]
49. Wintzer, M.; Nemec, M.; Aftosmis, M. Adjoint-Based Adaptive Mesh Refinement for Sonic Boom Prediction. In Proceedings of the 26th AIAA Applied Aerodynamics Conference, Honolulu, HI, USA, 18–21 August 2008. [CrossRef]